Solar Energy Materials & Solar Cells 254 (2023) 112292

Contents lists available at ScienceDirect

Solar Energy Materials and Solar Cells

journal homepage: www.elsevier.com/locate/solmat

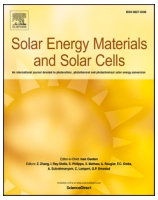

Development of Bi_2S_3 thin film solar cells by close-spaced sublimation and analysis of absorber bulk defects via in-depth photoluminescence analysis

M. Koltsov [a], S.V. Gopi [a], T. Raadik [a], J. Krustok [a], R. Josepson [b], R. Gržibovskis [c], A. Vembris [c], N. Spalatu [a,*]

[a] Department of Materials and Environmental Technology, Tallinn University of Technology, Ehitajate tee 5, Tallinn, Estonia
[b] Division of Physics, Tallinn University of Technology, Ehitajate Tee 5, 19086, Tallinn, Estonia
[c] Institute of Solid State Physics, University of Latvia, Kengaraga Str. 8, Riga, Latvia

ARTICLE INFO

Keywords:
Bismuth sulfide
Close-spaced sublimation
Thin film solar cells
Deep defects
Low-temperature dependence photoluminescence

ABSTRACT

The emergence of new PV applications in society requires the design of new materials and devices based on green and earth-abundant elements, with a different set of properties and wider applicability. In this perspective, Bi_2S_3 semiconductor material have gained attention as a defect-tolerant, non-toxic, and highly stable material for earth-abundant thin film PV technologies. Related to Bi_2S_3 non-toxic nature, so far it has been very popular to synthesize the material by chemical solution routes, while little research efforts have been dedicated to absorber deposition by physical deposition techniques. In particular, there are no studies on absorber development via rapid, high-volume, and in-line close-spaced sublimation technique. Moreover, in-depth analysis of material defects employing low temperature-dependent photoluminescence (PL) remains largely unexplored. In this work, we systematically study the impact of close-spaced sublimation (CSS) conditions on Bi_2S_3 absorber growth on various substrates, employing a wide range of source (400–600 °C) and substrate (200–400 °C) temperatures. CSS source temperature of 550 °C and substrate temperature of 400–450 °C were identified as optimal temperatures (grown either on glass, TiO_2, or CdS substrates), allowing the fabrication of uniform and dense Bi_2S_3 films with enhanced [221]-oriented grains. For the first time, a proof of concept solar cell with CSS Bi_2S_3 is demonstrated and an in-depth analysis on the interrelation between grain structure, interface recombination, and device performance is provided. Employing low-temperature dependence PL, new and complementary insights on possible defects and recombination mechanisms are presented.

1. Introduction

Bismuth chalcogenides (Bi-CAL) such as Bi_2S_3, Sb_2BiSe_3, $CuBiS_2$, $AgBiS_2$, and other related derivates are identified as a new class of emerging photovoltaic (PV) materials [1,2]. Bi_2S_3 material has a number of distinct advantages such as a high absorption coefficient (10^5 cm^{-1}, and absorption onset in the infrared) [1], exhibits both n-type [3] and p-type conductivity [4], bandgap lies in the optimal region for PV and can be varied from 1.1eV to 1.7 eV, due to quantum confinement effects and/or stoichiometry variations [1–4]. In addition, bismuth is an abundant metal on the Earth's crust; it is a by-product of Pb, Cu, and Sn refining and has significant commercial applications, resulting in the price of Bi being relatively low and stable [5,6]. Along with other emerging PV materials [2,7], bismuth is considered non-toxic and is even used in common medicines such as Pepto-Bismol [8]. Furthermore, Bi_2S_3 has been suggested as an excellent candidate for defect-tolerant compounds (i.e., materials with good optoelectronic properties despite the presence of defects); it crystallizes in the orthorhombic system where a 1D anisotropic lattice structure comprised of "nano-ribbons", held together via Van-der-Waals forces. This means no breaking of the lattice is required for termination at grain boundaries in Bi-CAL, making them grain boundary defect tolerant [1,2,9].

Defect tolerance is a key property of promising PV materials, especially for indoor PV applications where the defects in the PV can render a solar cell inoperable at indoor light levels. Despite of Bi-CAL PV material having this great advantage, its potential for indoor PV applications remains largely unexplored. Related to Bi_2S_3's non-toxic nature, so far it has been very popular to deposit the material by chemical solution routes such as chemical bath deposition [10], chemical vapor deposition (CVD) [11], metal-organic CVD (MOCVD) [12] as well and successive

* Corresponding author.
E-mail addresses: mykhailo.koltsov@taltech.ee (M. Koltsov), nicolae.spalatu@taltech.ee (N. Spalatu).

https://doi.org/10.1016/j.solmat.2023.112292
Received 2 November 2022; Received in revised form 23 February 2023; Accepted 13 March 2023

ionic layer adsorption and reaction (SILAR) [13]. Several reports demonstrated the potential of Bi-CAL materials in solar cells, using most often chemical methods, including colloidal Bi_2S_3 nanocrystals (NCs) [14,15], Bi_2S_3 active layer inorganic/inorganic bulk heterojunction solar cells (Bi_2S_3 nanowires) [16], Cu_3BiS_3 as a thin film [17] and sensitizer in dye-sensitized TiO_2 solar cells [18], and $CuBiS_2$ as nanoparticles [19]. Solar cell devices with a PCE of 5% have been realized by blending Bi_2S_3 NCs and PbS QDs to form a bulk nano-heterojunction structure which is the state of the art for such device architecture [15]. To date, the highest PCE for Bi-chalcogenide-based solar cell has approached 7% employing $Cu_4Bi_4S_9$ alloy as an absorber [20]. Significant research efforts were dedicated to the modification in the solar cell structure, however, this is not the only possible strategy to improve PCE. One significant drawback in all mentioned above Bi_2S_3 NCs-based heterojunction structures is that nanocrystals are randomly oriented in the films. Therefore, some of the NCs will be properly placed for conducting charges, while others will not, limiting charge transport and device PCE [1,12–15]. One strategy to overcome this limit is to take advantage of the naturally anisotropic, low-dimensional crystalline structures of Bi_2S_3 and to develop thin films with aligned 1D structures like nanoribbons. Such an approach will optimize the carrier transport through the growth of properly aligned and connected 1D ribbon structures and hence improve the thin film solar cell PCE. Although the such approach is widely used in other emerging chalcogenide PV materials with a similar 1D anisotropic ribbon structure like SnS, Sb_2Se_3, Sb_2S_3, and their alloys $Sb_2(S,Se)_3$ [21–24], it has been scarcely explored for Bi_2S_3, particularly for thin film device configuration.

Few strategies to create aligned Bi_2S_3 1D nanoribbon structures have been developed with bulk-heterojunction architectures achieving a promising 3.3% PCE [16]. The PCE of Bi-CAL-based solar cells is still low despite of predicted 30% theoretical PCE limit [1]. To make further progress in the PCE of Bi-CAL solar cells, absorber qualities such as composition morphology, crystallinity, crystallite orientation, bandgap, mobility, conductivity, carrier densities, doping density, and film density must be optimized. Also, the interfaces must be optimized to reduce the number of defects and recombination in a solar cell. Moreover, research investigations on the development of the Bi-CAL thin film as well as the solar cell structures by physical deposition methods are quite rare among the literature. Bi_2S_3 film was, supposedly, first deposited by physical methods in 1998 by Rincón et al. [10], heating the source material up to 900 °C and applying temperatures between 25 °C and 300 °C to the substrate. In the context of thin-film photovoltaic applications, Haaf et al. [25] employed physical deposition of Bi_2S_3 for the first time, ranging the temperature of substrate from 80 °C to 290 °C. | Therein by using confocal photoluminescence, the authors showed the advantages of high-temperature deposition in terms of optical properties. Song et al. [26] used rapid thermal evaporation to produce a Bi_2S_3 absorber layer for ITO/p-NiO/n-Bi_2S_3/Au solar cells, with source temperature around 600 °C and substrate temperatures between 100 °C and 300 °C, demonstrating a power conversion efficiency of 0.75%.

To the best of our knowledge, there are little to no reports in the literature regarding the deposition of Bi_2S_3 thin films and solar cells via close-spaced sublimation (CSS), which appeared to be a reasonable research gap to fill. In addition, there is a limited number of studies dedicated to defect analysis in the bulk of Bi_2S_3 thin films, employing advanced low-temperature dependence photoluminescence (PL) technique. In this context, the aim of the current study is to systematically investigate the impact of CSS processing conditions on the properties of Bi_2S_3 thin film absorber deposited on various substrates and to analyze the interrelation between the changes in the absorber properties and device performance. The novelty lies in the applied systematical technological approach, employing a large variation of the processing source and substrate temperatures, towards the identification of optimal CSS deposition conditions to produce uniform films with suitable orientation on various substrate partner layers. Comprehensive analysis of the structural and morphological changes in the absorber deposited on various substrates and correlation with the device efficiency is provided. Moreover, for the first time, we bring in-depth insights on defects and possible recombination mechanism in Bi_2S_3 absorber films employing low-temperature dependence photoluminescence measurements.

2. Experimental

2.1. Bi_2S_3 thin-film fabrication

Bi_2S_3 thin films were deposited atop of four different types of substrate: roughen microscopic glass (O.Kindler one end double frost microscopic glass, 1 mm thickness), plain glass (backside of Sigma-Aldrich FTO glass used, 2 mm thickness), glass/FTO/TiO_2, and glass/FTO/CdS stacks. CdS buffer layers were deposited onto Sigma-Aldrich FTO glass by a conventional chemical bath deposition (CBD) technique [27]. TiO_2 buffer layers were deposited on the same FTO glass by ultrasonic spray pyrolysis (USP) [28]. Bi_2S_3 films were deposited with a custom-made close-spaced sublimation (CSS) reactor from a Bi_2S_3 powder (Alfa Aesar, 5 N) under a vacuum of 10^{-4} Pa. To develop optimal CSS processing conditions which would allow fabricating of dense and compact absorber film, a systematical technological approach was adopted in which the CSS source temperature was varied between 450 °C and 600 °C, while for each source temperature, the substrate temperature was varied from 200 °C to 450 °C. The CSS temperature profile and ramping are schematically presented in Fig. 1.

2.2. Material and device characterization

X-ray diffraction (XRD) patterns were taken using a Rigaku Ultima IV diffractometer with Cu Kα radiation (λ = 1.54 Å, 40 kV, 40 mA). A Zeiss HR-SEM MERLIN scanning electron microscope (SEM) with the GEMINI II column was used for the top- and cross-sectional view of the structures. Raman measurements were performed with a Horiba Jobin Yvon Labram HR 800 spectrometer (λ = 532 nm). The resistivity, charge carrier concentration, and mobility of the Bi_2S_3 films were measured at room temperature using MMR's variable-temperature Hall system and a Hall and van der Pauw controller H-50. The in-plane resistivity and electron densities were calculated for thicknesses of 0.5–1 μm, which were estimated from the SEM analysis. Each measurement was carried out 5 times and the mean value was taken. J-V curves were measured for Bi_2S_3 devices with a Wavelabs LS-2 LED solar simulator (100 mW cm^{-2}, AM1.5) at room temperature in ambient air. External quantum efficiency (EQE) spectra were measured with a monochromatized light source (Newport 300 W Xenon lamp, Newport Cornerstone 260 monochromator), a Merlin digital lock-in detector, and a factory-calibrated Si reference detector. The ionization potential and electron affinities of the thin films in the device stack were determined by the photoelectron emission spectroscopy technique, to ascertain the band alignment. A 0.64 m focal length single grating (600 mm^{-1}) monochromator and the 442 nm line of a He–Cd laser with different powers were used for PL measurements. For PL signal detection, a Hamamatsu InGaAs photomultiplier tube (PMT) was used. A closed-cycle helium cryostat was employed to measure temperature dependencies of the PL spectra at temperatures from 20 to 300 K. The laser spot size for these measurements was 200 μm in diameter.

3. Results and discussion

3.1. Structural properties of Bi_2S_3 films

Bi_2S_3 films deposited by CSS onto four different substrates – roughen microscopic glass, plain glass on the backside of FTO substrate, glass/FTO/TiO_2 (further just TiO_2), and glass/FTO/CdS (further just CdS) stacks. A large series of Bi_2S_3 absorber layers were initially deposited on roughen glass substrate with the aim to identify the most optimal CSS source (T_{so}) and substrate temperatures (T_{sub}) which would allow a

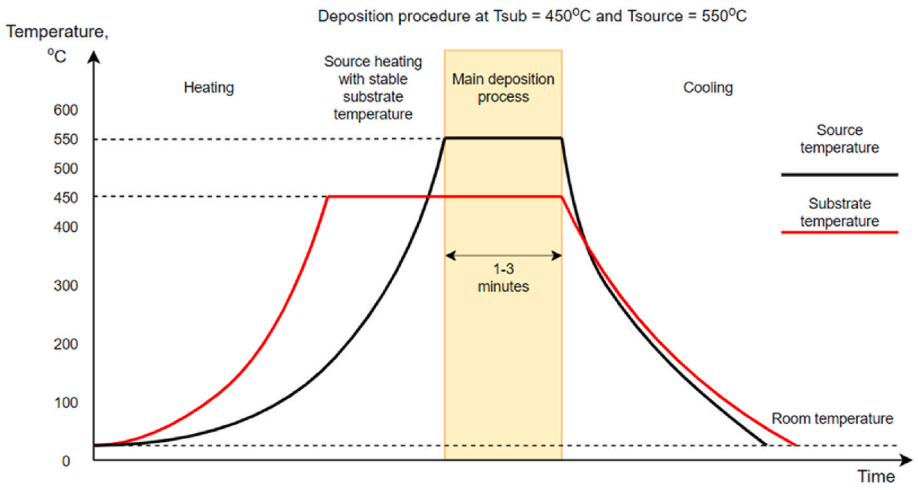

Fig. 1. Schematic representation of the CSS deposition temperature profile and ramping.

reasonable deposition rate and lead to the formation of compact and dense films. The roughened glass plates with a root-mean-square roughness, Rq, of 2.66 nm (Sigma-Aldrich) were used to ensure better adhesion of the Bi_2S_3 absorber films and also to perform electrical measurements. After the identification of the optimal source temperature, the absorber was deposited onto different substrates (including plain glass, TiO_2/FTO/glass, and CdS/FTO/glass substrates) with the variation of the substrate temperature between 200 and 450 °C in steps of $\Delta T = 50$ °C. Information about deposition conditions for different substrates is summarized in Table 1. All Bi_2S_3 films deposited on various substrates were first characterized by XRD and Raman spectroscopy. Fig. 1 (a,c,e) shows XRD patterns of Bi_2S_3 films deposited onto roughen glass, which were indexed and assigned to orthorhombic Bi_2S_3 crystal structure with *Pbnm* space group symmetry (JCPDS 00-017-0320) [29].

For a better qualitative analysis of the preferential orientation of the crystallite along specific crystalline planes, the texture coefficient (TC) was calculated (Fig. 2b,d,f) according to Eq. (1):

$$TC(hkl) = \frac{I(hkl)}{I_0(hkl)} \times \left[\frac{1}{N}\sum_{i=0}^{N}\frac{I(hkl)}{I_0(hkl)}\right]^{-1} \quad (1)$$

where *I(hkl)* is the measured intensity for a given reflection with *hkl* indices, *I0(hkl)* is a reference intensity for a given reflection acquired from the JCPDS Card No. 00-017-0320, and *N* is the number of reflections considered in the analysis [30].

It can be seen that for a given T_{so}, the values of TC change differently depending on T_{sub}. At T_{so} 500 °C, (020) and (130) crystalline planes were dominant. When the T_{sub} was increasing, the values of TC increased for (020) and (130) planes, and at the same time along other major planes like (220) and (211), the TC values decreased. In the case of T_{so} 550 °C, the most prominent planes were (130), (310), and (211). Generally, it was difficult to distinguish some clear trend for the TC of (020), (220), and (130) planes, while the TC for (310), (211), and (221) planes had slightly grown along with the increase of T_{sub}. At T_{so} 600 °C, the most prominent planes were (310), (211), and (221) for which the TC values increased systematically when the T_{sub} increased from 200 to 350 °C. For the same T_{so}, at substrate temperatures higher than 350 °C the TC values of the same planes decreased.

Table 1
Deposition conditions for various substrates.

Substrate	Roughen glass	Plain glass	TiO_2	CdS
T_{so}, °C	450, 500, 550, 600	550	550	550
T_s, °C	100–550	200–450	200–450	200–450
Deposition time, min	1	1, 2, 3, 5	1	1

For the next set of samples in which the Bi_2S_3 films were deposited on glass, CdS, and TiO_2, the T_{so} 550 °C was chosen as the optimal source temperature, allowing an optimal deposition rate of ~0.8–1 μm/min. The choice for this temperature was also made based on a systematic source temperature screening for different substrates and according to XRD data the 550 °C source temperature led to the most prominent orientation of the crystallite along (*hkl*, $l = 1$). In addition, when compared to T_{so} 600 °C, the T_{so} 550 °C also allowed better controllability of CSS deposition process and absorber layer thickness.

When performing the TC analysis of Bi_2S_3 deposited onto plain glass substrates at T_{so} 550 °C, no clear trend was found, except the decreasing of TC for the (221) plane with the increasing of substrate temperature from 250 to 450 °C. At the same time, in comparison with the films deposited onto rough glass there is a difference in the TCs of the films grown onto plain glass. This effect can be explained by different surface energy of these two substrates. In the case of rough glass, the higher surface energy can provide different conditions for the nucleation sites and adatom diffusion on the surface. This will affect the formation of islands, their coalescence and grain coarsening during the film growth and thus the orientation of the final grains in the layers. For the absorber deposited on TiO_2 substrates, with an increase in the substrate temperature, the TC were slowly decreasing for the (020), (220), (130), and (310) planes while increasing for the (221) plane. In the case of Bi_2S_3 films deposited on CdS substrate, the TC was slowly decreasing for (130) and (211) planes and increasing for (310) and (221) planes, as the substrate temperature increased from 250 to 450 °C (see Fig. 3). It is important to mention that according to XRD results, at T_{so} below 500 °C the film seemed mostly amorphous with very few distinguishable peaks (Fig. S1, Supplementary material). On another hand, a very interesting observation is that in the XRD pattern of Bi_2S_3 deposited with T_{so} ~600 °C and T_{sub} ~450–500 °C, separated phases of Bi and Bi_2S_3 were detected (Fig. S2, Supplementary material), suggesting that at higher deposition temperature there was an excessive loss of sulfur from the system. Such a phenomenon can be explained by the higher partial pressure of sulfur at $T \geq 600$ °C which can easily generate sulfur poor conditions in the Bi_2S_3 system [31]. It should be noted that the phase composition of Bi_2S_3 was further analyzed by Raman measurements, as seen in Fig. S3, Supplementary material. For the T_{so} 550 °C, independent of the substrate temperature and the used substrate for the deposition of Bi_2S_3 films, Raman spectra showed similar vibrational modes, which correspond to the pure Bi_2S_3 phase [32].

Bi_2S_3 absorber films, deposited on all substrates, at low (250 °C) and high (450 °C) temperatures, were analyzed by scanning electron microscopy (SEM). Images of Bi_2S_3 films, deposited onto roughen glass, are given in Fig. 4. It can be seen, that absorber layers deposited at higher

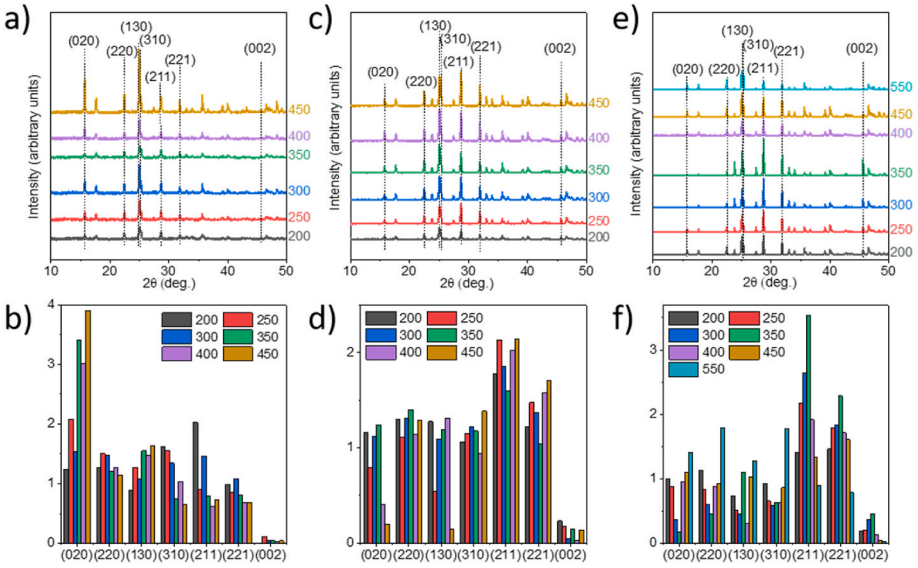

Fig. 2. XRD patterns of Bi_2S_3 absorber films deposited by CSS onto roughen glass substrates, at three source temperatures (T_{so}) – (a) 500 °C, (c) 550 °C, (e) 600 °C, and for each T_{so}, the substrate temperature varied between 200 °C and 550 °C in steps of $\Delta T = 50$ °C; (b, d, e) The corresponding TC values calculated from integrated intensity ratios for main crystal planes in Bi_2S_3 films.

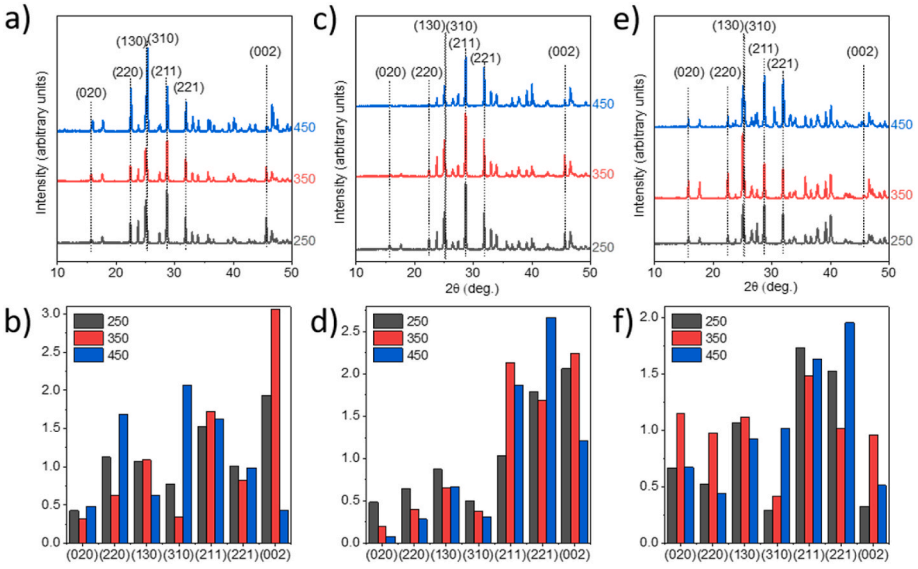

Fig. 3. XRD patterns of Bi_2S_3 absorber films deposited by CSS at T_{so} 550 °C and T_{sub} 250 °C, 350 °C and 450 °C onto various substrates – (a) plain glass, (c) TiO_2 and (e) CdS; (b, d, e) TC values calculated from integrated intensity ratios for main crystal planes in Bi_2S_3 films on respective substrates.

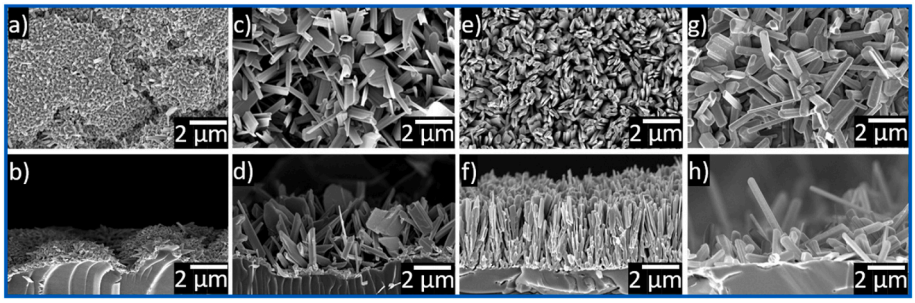

Fig. 4. (a, c, e, g) Top-view and (b, d, f, h) cross-sectional SEM images of Bi_2S_3 films deposited onto a roughen glass substrate at substrate temperature (T_{sub}) of (a, b) 200 °C, (c, d) 250 °C for 1 min deposition time, (e, f) T_{sub} of 250 °C for 3 min deposition time, and (g, h) T_{sub} of 450 °C for 1 min deposition time.

temperatures consists of larger grains compared to the films obtained at low-temperatures.

At 200 °C, the surface of the substrate was covered with a ~200 nm thick "seed" layer of small randomly-oriented grains (Fig. 4a and b). At higher temperatures (200–350 °C), needles and prism-like grains with no dominating orientation of growth were observed out of a minor portion of the seed layer (Fig. 4c and d). If deposition time in this temperature region was prolonged, more and more grains from the seed layer were able to grow into a needle (Fig. 4e and f). These needles were growing higher and more aligned as the thickness of the film increases from 3-4 μm to 4–5 μm, resulted from a change in the deposition time from 1 min (Fig. 4d) to 3 min (Fig. 4f). At high temperatures (400–450 °C), grains tend to coalesce, forming big randomly oriented "rods", while the previously-existing seed layer is not visible anymore (Fig. 4g and h).

In the case of Bi_2S_3 deposited on plain glass, fewer nucleation centers were available on the substrate surface. This implies that a higher minimal T_{so} was required for the appearance of a first Bi_2S_3 thin film, compared with roughen glass - approximately 420 °C for roughen and 470 °C for plain glass substrates. At T_{so} 250 °C, the Bi_2S_3 films grow in a similar way to a film on roughen glass (Fig. 5a and b). At T_{so} 450 °C, a densely-packed morphology was observed in which grains grow in both lateral and longitudinal directions (Fig. 5c and d). In the case of prolongated deposition time, ~200 nm and ~600 nm thick films were obtained for 3 min (Fig. 5e and f) and 5 min (Fig. 5g and h) deposition time, respectively.

For Bi_2S_3 films, deposited on plain glass, TiO_2, and CdS at T_{sub} 250 °C, a similar morphology in which the films consisted of randomly-oriented needles and wide distribution by size (0.5–6 μm) was observed. At T_{sub} 450 °C, thick films of large, rather columnar grains were observed (Fig. 6d,h), with a similar formation mechanism seen in Fig. 5h. As a result of 1 min deposition, ~1 μm thick Bi_2S_3 films were observed onto TiO_2 and CdS substrates, while five times thinner (200 nm) film was observed on plain glass after 3 times longer deposition. The thicker film on TiO_2 and CdS can be explained by a higher nucleation sites density on the surface of both TiO_2 and CdS. It should be mentioned, that EDX analysis was conducted, focusing on the compositional maps of the cross section to check the homogeneity of the elemental distribution. No metallic elements or micro-inclusions of secondary phases were detected in the Bi_2S_3 films deposited at T_{so} 550 °C (Figs. S4 and S5, Supplementary material).

Based on the results of structural and morphological changes of Bi_2S_3 absorber layers depending on the CSS deposition conditions and use of various substrates, the following main conclusions can be drawn:

i. Within the given set of source and substrate temperature regimes (T_{so}: 450 °C, 500 °C, 550 °C, and 600 °C; T_{sub}: 250 °C, 450 °C), the source temperature of 550 °C and substrate temperature 400–450 °C were identified as optimal temperatures which allowed reasonable deposition rate (~0.5–0.8 μm/min) and fabrication of uniform Bi_2S_3 films with a suitable (*hkl*, $l = 1$) orientation independent whether the deposition was performed on either plain glass, TiO_2 or CdS as substrate;
ii. At T_{so} below the optimal one, independent of the applied substrate temperatures, the absorber grains were predominantly oriented along (*hkl*, $l = 0$), while a high amount of amorphous phase was observed in Bi_2S_3 film grown at T_{so} 450 °C;
iii. 600 °C source temperature was identified as a critical temperature, generating conditions for sulfur loss in the Bi_2S_3 system with the formation of separated metallic bismuth and Bi_2S_3 phases.

It is widely established for similar emerging inorganic chalcogenides such as Sb_2S_3 and Sb_2Se_3 absorbers that such a preferential (*hkl*, $l = 1$) orientation, obtained at T_{so} 550 °C and T_{sub} 450 °C for Bi_2S_3 film would be optimal for efficient charge transport and collection in the solar cell [33–36]. At this point, it is worth mentioning that several attempts investigated the properties of Bi_2S_3 deposited via physical deposition methods. Employing a thermal evaporation technique at T_{sub} between 25 °C and 285 °C, Haaf et al. [25] found that Bi_2S_3 films grown at temperatures right above the crystallization temperature exhibit a significant overrepresentation of reflections with indices (*hkl* $l = 0$), with a preferred growth along the c-axis parallel to the surface of the substrate. Therein only structural and optical properties were analyzed without the application of the absorber layer in a solar cell device. Following the same technological approach, Rincón et al. [10] obtained crystalline Bi_2S_3 film at T_{sub} 250–300 °C, however, with strong contribution in XRD patterns from (104), (012), and (003) planes of metallic bismuth. Therein the appearance of the separated phase was explained due to the nonstoichiometric dissociation of the S/Bi precipitate. Using a rapid thermal evaporation technique with a fast deposition rate (0.5 μm/min) at T_{sub} 100–300 °C, Song et al. [26] obtained crystalline, (023) (111) (122) oriented, compact Bi_2S_3 films. So far, this is the only study in which the Bi_2S_3 film deposited by physical deposition method was incorporated in solar cells with a demonstration of proof-of-concept device efficiency of 0.75%.

In terms of CSS processing temperature, our results seem to correlate with the findings by Song et al. [26], with the difference that in our case the optimal growth condition identified at a slightly higher substrate temperature and a general trend for the TC favorable towards grain orientation along (*hkl*, $l = 1$) planes. Having noticed these findings, the next challenge in this study was to apply the absorber, processed with the identified optimal T_{so} and T_{sub}, in a superstrate configuration solar cell with TiO_2 or CdS as the junction partner layer.

3.2. Bi_2S_3 device efficiency: analysis of the performance limitations

Based on the above analysis of the systematical structural changes in the Bi_2S_3 film growth depending on the CSS source and substrate deposition temperatures, we further analyzed how these structural changes correlate with the efficiencies of superstrate configuration glass/FTO/CdS/Bi_2S_3/Au and glass/FTO/TiO_2/Bi_2S_3/Au thin film solar cells. Fig. 7a show the schematic of the two device configurations

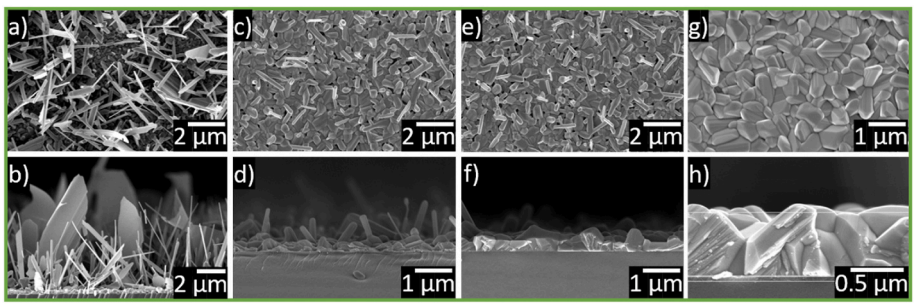

Fig. 5. (a, c, e, g) Top view and (b, d, f, h) cross-sectional SEM images of Bi_2S_3 films deposited onto a plain glass substrate at: (a,b) substrate temperature (T_{sub}) of 250 °C for 1 min deposition time; T_{sub} 450 °C at (c,d) 1 min, (e,f) 3 min, and (g,h) 5 min deposition time.

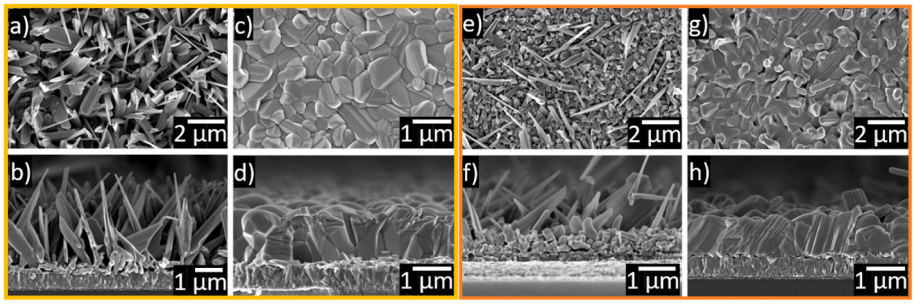

Fig. 6. (a, c, e, g) Top view and (b, d, f, h) cross-sectional SEM images of Bi_2S_3 films deposited onto (a–d) TiO_2 and (e–h) CdS substrates, at substrate temperature (T_{sub}) of (a-b, e-f) 250 °C and (c-d, g-h) 450 °C, deposition time is 1 min.

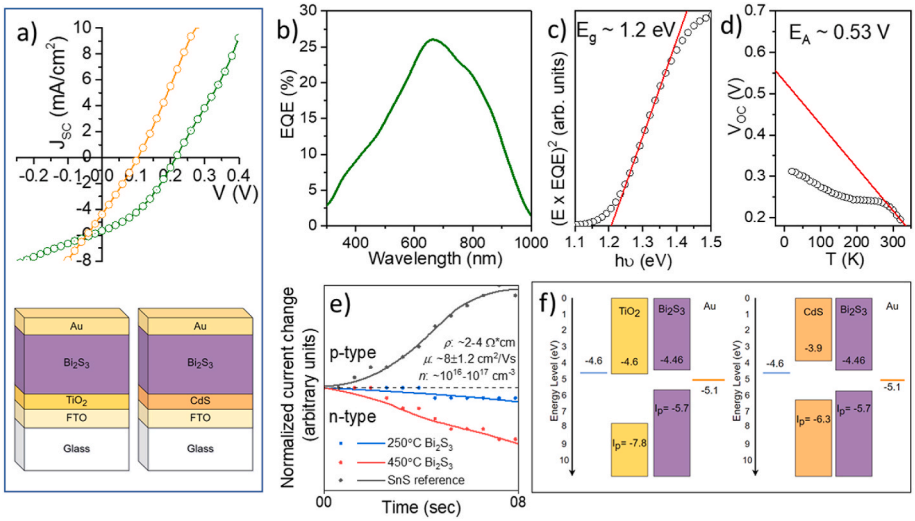

Fig. 7. a) Superstrate schematic configuration of the glass/FTO/CdS/Bi_2S_3/Au and glass/FTO/TiO_2/Bi_2S_3/Au thin film solar cells and representative J-V characteristics for the best devices (orange curve for CdS/Bi_2S_3, and green curve for TiO_2/Bi_2S_3). b) and c) Respective EQE spectral response and related modified EQE plot, giving a band gap estimation of 1.2 eV of Bi_2S_3 at RT. d) V_{OC} temperature dependence together with the extrapolation to 0 K for the estimation of the activation energy (E_A). e) hot-probe and relevant results of the Hall measurements of the carrier type and electron concentration in Bi_2S_3 thin film absorber. f) Band offsets with the estimation of the ionization energies for two configuration devices, measured via photoelectron emission spectroscopy method.

together with the representative *J-V* characteristics for the best devices, both of them processed with Bi_2S_3 absorber deposited at 450 °C. It can be seen that the TiO_2/Bi_2S_3 cell exhibit better efficiency compared to CdS/Bi_2S_3 device. A set of 5 cells (0.5 cm^2 contact area) were fabricated for each device structure, leading to an average device performance of $\eta \sim 0.1 \pm 0.05\%$ (with $V_{OC} \sim 90 \pm 10$ mV, $J_{SC} \sim 3.5 \pm 0.7$ mA/cm^2, and $FF \sim 23.0 \pm 0.3\%$) and $\eta \sim 0.3 \pm 0.05\%$ (with $V_{OC} \sim 190 \pm 10$ mV, $J_{SC} \sim 4.6 \pm 0.8$ mA/cm^2, and $FF \sim 32.0 \pm 0.3\%$) for CdS/Bi_2S_3 and TiO_2/Bi_2S_3, respectively. For the latest configuration, the highest achieved efficiency was $\eta \sim 0.45\%$, with $V_{OC} \sim 210$ mV, $J_{SC} \sim 5.7$ mA/cm^2, and $FF \sim 38\%$. For both device configuration, processed with Bi_2S_3 at CSS substrate temperatures below 400 °C, the efficiencies tend to be zero. The EQE of the best device (Fig. 7b) shows quite modest response throughout the whole wavelength interval, in correlation with the representative *J-V* characteristics (Fig. 7a). The modified EQE plot (Fig. 7c) gave a band gap estimation of $E_g \sim 1.2$ eV for Bi_2S_3 at room temperature, in agreement with the values reported in the literature [37].

So far, these results indicate that the morphology of Bi_2S_3 has an impact on the cell performance, however, the modest TiO_2/Bi_2S_3 cell efficiency (which incorporates an absorber with larger and compact grains, Fig. 6d) clearly indicates that there are other factors which drastically affects the final cell performance. On one hand, the low EQE response suggests that the carrier collection at the contacts is well reduced. Moreover, it also indicates low carrier collection close to the buffer-absorber interface (i.e., high recombination velocity at the interface and small diffusion length of the minority carriers in bulk) [38]. The last argument is also supported by the activation energy value of $E_A \sim 0.53$ eV, obtained from V_{OC} temperature dependence (Fig. 7d). This value is well below the bandgap energy, indicating that the interface recombination has a significant role in limiting the V_{OC} of these devices. On another hand, it is well known that the conductivity type and carrier concentration in the absorber, together with the buffer–absorber band offset also play a significant role in the formation of the heterojunction interface and resulted space charge region (SCR). The width of the SCR at the heterojunction interface depends on many factors, but among them, the carrier concentration in both, buffer and absorber layers have a key role. The conductivity type and carrier concentration of the Bi_2S_3 absorber layers deposited on glass substrates were analyzed by the hot-point probe and Hall measurements, respectively (Fig. 7e). For the hot probe analysis, SnS thin film deposited by CSS on the same glass substrates was used also as a good p-type reference [39]. Independent of the CSS deposition temperatures, the Bi_2S_3 absorber layers always showed n-type conductivity with an electron concentration of $n \sim 10^{16}$-10^{17} cm^{-3} and electron mobilities of 4.0 ± 0.8 cm^{-3} and 8.0 ± 1.2 cm^{-3}, for the films deposited at T_{so} 550 °C and T_{sub} 250 °C–450 °C, respectively. These results imply that both CdS/Bi_2S_3, as well as TiO_2/Bi_2S_3, are described as an n-n isotype heterojunction. The high values of the electron density in the absorber imply that the SCR is very narrow and most likely extends into the buffer layer, at the heterojunction interface, leading to ineffective charge separation, and high recombination rates. All these effects justify the poor performance of the CdS and TiO_2-based devices. In the case of both, n-n isotype and n-p heterojunctions, for the n-type layer, the electron density should be 1–2 orders of magnitude above the carrier concentration in the absorber material. This would allow an efficient charge separation and transport assuming the existence of a suitable 0.2–0.4 eV conduction band spike offset between the buffer and absorber layers [40]. In addition, the n-n

isotype heterojunction device will be very sensitive to the band offset and formation of the related interface defect state density. The ionization energy values for the constituent layers in the solar cell stack were obtained from photoelectron emission spectroscopy measurements. Fig. 7f shows the band energy diagrams of CdS/Bi_2S_3 and TiO_2/Bi_2S_3 solar cells with estimated values of the ionization energies. For the CdS/Bi_2S_3 device, the formation of a "spikelike" band offset can be assumed, as the conduction band minimum (CBM) of the CdS buffer layer lies above the CBM of the absorber [41]. In this case, the too-positive offset of the CdS CBM (~0.5 eV) creates a potential barrier for the excited electrons in the Bi_2S_3 absorber, opposing their drift into the buffer layer and thereby drastically lowering the J_{SC} and hence, the efficiency of device (Fig. 7a). In the case of TiO_2/Bi_2S_3 device, however, the formation of a "clifflike" offset can be distinguished (Fig. 7f) in which the CBM of the TiO_2 film lies below that of the absorber. For a such band alignment, the back-transfer carrier recombination at the main interface, in which the electrons in the TiO_2 film recombine with holes in the Bi_2S_3 absorber via interface states, is more likely. The latest phenomenon limits the built-in voltage of the heterojunction and hence the V_{OC} and efficiency of the cell.

The above solar cell results and related analysis indicate that the TiO_2/Bi_2S_3 device is described as n-n isotype heterojunction and among all the aforementioned limitations effects, the high electron concentration determined by the defects in the bulk of the absorber together with recombination at the main interface are the most detrimental. In this regard, temperature-dependence admittance spectroscopy can provide more insights on defect features in the Bi_2S_3 absorber. However, our attempts to perform such measurements failed, as for such a low-quality n-n type heterojunction it was difficult to detect the inflection frequency in the admittance spectrum. However, we succeeded to perform low-temperature dependence spectra, as described in the following 3.3 section.

3.3. Unveiling defects and possible recombination in Bi_2S_3 absorber from photoluminescence analysis

To explore the existence of possible defects in Bi_2S_3, low-temperature photoluminescence (PL) spectra were measured for Bi_2S_3 absorber layers deposited onto glass, CdS/FTO/glass, and TiO/FTO/glass stacks. It is worth mentioning that there are a very limited number of reports in the literature on PL studies of Bi_2S_3 thin films deposited by physical deposition techniques. As it has been more popular to synthesize Bi_2S_3 using chemical deposition methods, several reports employed room temperature PL analysis for Bi_2S_3 nanowires [42], nanoleafs [43], nanoparticles, and complex nanostructures [44,45], as well as for the Bi_2S_3 heterojunction-based structures for photocatalytic and hydrogen productions applications [46]. Related to Bi_2S_3 films processed by physical deposition methods, only two relatively recent studies by Haaf et al. [25] and by Jamali et al. [47] reported room temperature PL analysis. Employing confocal photoluminescence spectroscopy, Haaf et al. proved the advantages of the high-temperature deposition range for optical properties and therefore suggest, together with the results from both surface analysis and conductivity measurements, the preparation of solar cell structures at temperatures ≥240 °C during Bi_2S_3 deposition. Jamali et al. performed room temperature PL analysis for Bi_2S_3/SnS thin film heterojunction-based photodetector. Therein the authors assigned several two PL emissions with bismuth vacancy (V_{Bi}) and sulfur interstitials (Si). However, in both aforementioned studies, the PL was not performed at low temperatures and hence, no in-depth analysis of possible defect-related transitions was discussed. Therefore, we aimed to perform a systematic analysis of low-temperature PL and temperature PL study in CSS Bi_2S_3 thin films and provide a correlation between defect features in the absorber and the performance of the solar cell device. For simplicity, the temperature dependence PL spectra of Bi_2S_3 deposited on glass, CdS/FTO/glass, and TiO/FTO/glass stacks are presented in Fig. S6, Supplementary material. Fig. 8a shows the PL spectra measured at 100 K for the Bi_2S_3 deposited at 400 °C onto TiO_2/FTO substrate. For this specific configuration, the highest PL yield was obtained and therefore the analysis was focused on this sample but in general, the results can be extrapolated for the whole series of investigated structures. Looking at Fig. 8 (a) the broad PL band indicates to the presence of a high concentration of defects in the Bi_2S_3 absorber layer. The best fitting was achieved considering three bands labeled as B1 – main emission, at 1.13 eV, B2 – at lower energies, 0.86 eV, and B3 – at higher energies, 1.23 eV.

To further understand the origin of these three emissions, the displacement of the band's positions depending on the measurement temperature was analyzed. Fig. 8b–d shows this dependence for all three bands and it can be observed that all the bands follow almost the same trend with increasing temperature, distinguishing three regions: region–(I) low-temperature region, 10–75 K, in which the band position shifts towards lower energies; region–(II) between 75 K and 100 K, where the band position does not change; and region–(III) high-temperature region, 100–150 K, in which the band position shifts towards higher energies. Such behavior in the temperature dependence of band position has been observed in other materials [48] and indicates the implication of phenomena such as band-to-impurity transition in the presence of potential fluctuations in the materials and/or transitions within deep donor-deep acceptor (DD-DA) pairs.

To assign one of these models, each band (B1–B3) should be analyzed separately, including additional laser power dependence measurements. For the main B1, laser power dependence (Fig. 8e) shows a very small shift of about three meV per decade. Such a small shift is possible in the case of Deep Donor – Deep Acceptor (DD–DA) recombination. For shallow D–A pair it is expected a higher shift, of ~10 meV per decade, while for the band to impurity transition, even a higher shift is expected, ≥20 meV. The activation energy of ~53.0 ± 0.2 meV was determined from the Arrhenius plot of the resulting integral intensities for B1. Similar activation energies around 50 mV were obtained for the B1 PL band of Bi_2S_3 deposited on glass and CdS/FTO/glass substrates, presented together with the respective temperature dependence PL spectra in Fig. S6, Supplementary material. If to assume the implication of potential fluctuation in the material, then the activation energy should be in the range of ~120 meV, so that to satisfy the correlation between band gap energy (~1.2 eV) and activation energy of the respective B1-related band emission. Here, this seems not to be the case, thus the DD–DA still remains the most probable recombination mechanism related to B1. In addition to this argument, the B1 band shape is quite symmetric which also excludes the implications of potential fluctuation. Related to B2 emission, its broadness and small intensity suggest that it is still related to deep defects, since it is still energetically far from the bandgap energy, about 350–370 meV from the bandgap energy. Looking at the B3 emission, it has a very small intensity and it is more prominent at higher temperatures. Considering its position at 1.23 eV, it could be related to band-to-band emission.

Coming back to the analysis of B1 emission, a natural question that arises then is how the presence of DD–DA recombination correlates with the electrical properties of Bi_2S_3 presented above. The obtained relatively high electron concentration of 10^{16}–10^{17} cm^{-3} clearly indicates to the presence of shallow donors in Bi_2S_3 absorber films. A pertinent answer would be that this DD–DA involved in the B1 emission is a neutral complex that does not have an impact on the electrical properties. The initial donor is deep and the initial acceptor is also deep, and only for the closely separated DD–DA pairs the energy is decreasing, resulting in a rather small activation energy obtained in Fig. 8f. As a rule of thumb, this activation energy (~53 meV) is attributed to a shallow acceptor, as the PL temperature quenching in most of the materials is related to the acceptor level. From a theoretical perspective, the first-principles DFT calculations provide a larger variety of defects in Bi_2S_3 [37]. The donor defects such as vacancies of sulfur (V_S) have much lower formation energies, under both, Bi-rich and S-poor or under the Bi-poor and S-rich conditions [37]. Thus, n-type conductivity and higher

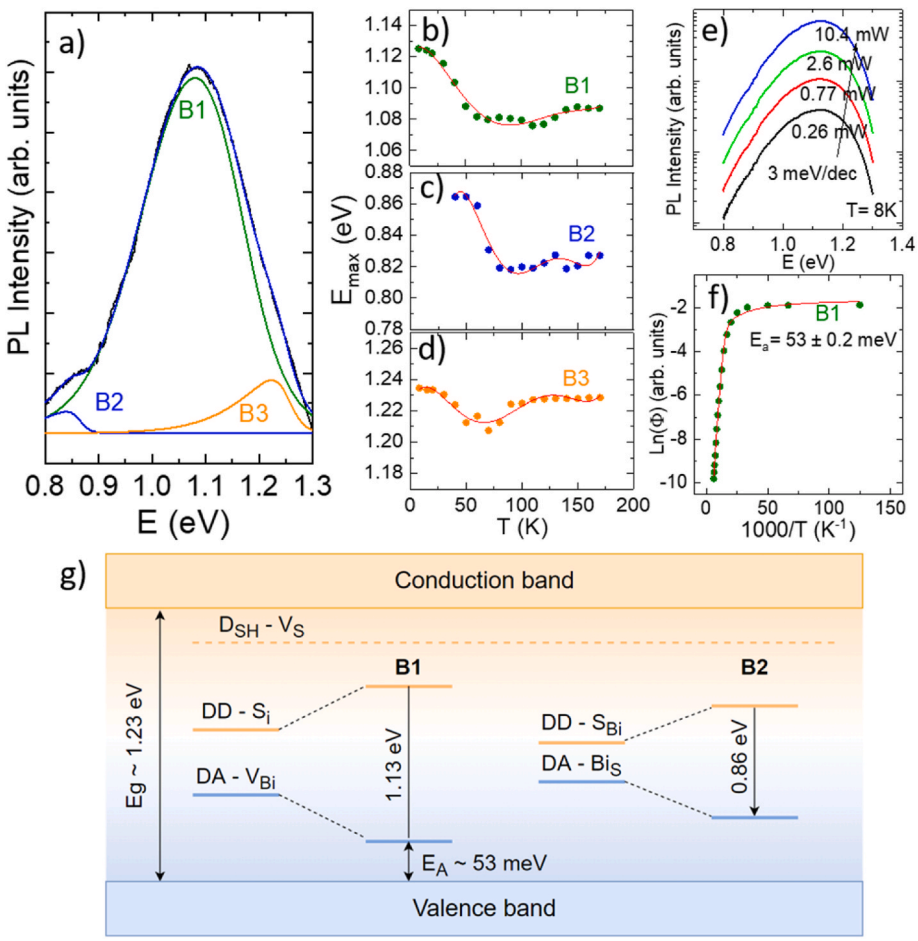

Fig. 8. (a) Photoluminescence spectrum at 100 K, for Bi_2S_3 absorber layer deposited on top of TiO_2/FTO/glass substrate; the best fitting was achieved with three bands: B1 at 1.13 eV (green), B2 at 0.86 eV (blue), and B3 at 1.23 eV (orange). b-d) Shift of each band position depending of the measurement temperature. e) Laser power dependence of the low-temperature B1 PL band, showing a shift of ~3 meV per decade. f) Arrhenius plots of the integral intensity of the B1 PL band with the fitting result. g) Proposed Deep-Donor to Deep Acceptor (DD-DA) recombination model for Bi_2S_3 absorber films at 8 K. The D_{SH} – V_S label in the diagram designates the sulfur vacancy shallow donor.

electron concentration are usually expected in Bi_2S_3. Interestingly, most of the intrinsic point defects act as donors, even the anion interstitial sulfur (S_i), which is usually an acceptor in other chalcogenide semiconductors [39], acts as a donor. Only vacancies of bismuth (V_{Bi}) and antisite Bi_S act as acceptor defects [37], but both these defects are very deep (high) within the bandgap, close to the conduction band minimum so that their ionization does not occur effectively in order to generate higher concentration hole carriers. Thus, this defect configuration makes p-type doping in Bi_2S_3 quite challenging. Based on the above PL analysis and considering the aforementioned possible formation of defects in Bi_2S_3, a model of the DD–DA recombination mechanism is proposed in Fig. 8g. For the B1 emission, the DD and DA were assigned to S_i, and V_{Bi}, respectively while the B2 band was attributed to the second DD–DA pair (next closest distance) implying a deeper donor and acceptor of S_{Bi} and Bi_S, respectively. At the same time, it is also possible that the B2 band is related to the same the DD–DA pair as for the B1 band (i.e. the initial positions of defect levels will be the same), but with a larger distance between DD and DA in the lattice, resulting in slightly deeper energy levels for the DD–DA pair. Such high concentration of defects involving deep pair complex configuration, explains why the efficiencies of the respective isotype heterojunction CdS/Bi_2S_3 and TiO_2/Bi_2S_3 solar cells are so modest. These results are good agreement with the first-principle theoretical predictions [37] in which the high concentration of point defects (such as Bi_S, V_S, or S_{Bi}, S_i) in Bi_2S_3 can produce deep levels in the band gap and act as electron-hole recombination centers, decreasing the lifetime of the minority carriers and the efficiency of the solar cell. A carrier lifetime in the orders of 10–50 ps [37] would be even more critical for a n-n type heterojunction with a very weak electric filed. Thus, the development of p-n heterojunction Bi_2S_3 solar cells [15] can facilitate the electron-hole separation by the build in electric field and thus increase the carrier lifetime as well as the performance of the solar cell device. Implementation of possible processing strategies such as p-type doping of the absorber together with identification of alternative optimal heterojunction partner layer with suitable band offset remains largely unexplored approaches for this material and could offer new perspectives to improve the performance of Bi_2S_3 thin film solar cells.

4. Conclusions

In conclusion, we systematically studied the impact of CSS processing conditions on the properties of Bi_2S_3 thin film absorber deposited on various substrates and analyzed the interrelation between the changes in the absorber properties and device performance. The source temperature of 550 °C and substrate temperature of 400–450 °C were identified as optimal temperatures which allowed a reasonable deposition rate (~0.5–0.8 μm/min) and fabrication of uniform Bi_2S_3 films with a suitable (*hkl*, $l = 1$) orientation independent whether the deposition was performed on either plain glass, TiO_2 or CdS as substrate. At T_{so} below the optimal one, independent of the applied substrate temperatures, the absorber grains were predominantly oriented along (*hkl*, $l = 0$), while a high amount of amorphous phase was observed in Bi_2S_3 film grown at source temperature 450 °C. 600 °C source temperature was identified as a critical temperature, generating conditions for sulfur loss in the Bi_2S_3 system with the formation of separated metallic bismuth and Bi_2S_3 phases. For the source temperature 550 °C, independent of the substrate temperature and the used substrate for the deposition of Bi_2S_3 films, Raman spectra showed similar vibrational modes, which correspond to the pure Bi_2S_3 phase. For the first time, a proof of concept of 0.45% efficient solar cells incorporating CSS Bi_2S_3 absorber layer is

demonstrated and an in-depth analysis of the interrelation between grain structure, interface recombination, and device performance is provided. Independent of the CSS deposition temperatures, the Bi_2S_3 absorber layers always showed n-type conductivity with an electron concentration of $n \sim 10^{16}$-10^{17} cm^{-3} and electron mobilities of 4.0 ± 0.8 cm^{-3} and 8.0 ± 1.2 cm^{-3}, for Bi_2S_3 deposited at 250 °C and 450 °C, respectively. These results imply that both CdS/Bi_2S_3, as well as TiO_2/Bi_2S_3, are described as an n-n isotype heterojunction in which the space charge region is very narrow and most likely extends into the buffer layer, at the heterojunction interface, leading to ineffective charge separation, and high recombination rates. V_{OC}-T analysis of the device indicated that the interface recombination is one of the major limitations in the efficiency of the solar cell. The analysis of energy level alignment via photoelectron emission spectroscopy technique suggests the formation of a "spikelike" band alignment and a "clifflike" offset for CdS/Bi_2S_3 and TiO_2/Bi_2S_3 devices, respectively. Such energy level alignment implies limitations in the device performance due to a potential barrier and back-transfer carrier recombination at the main interface. Low-temperature dependence PL analysis shows the presence of three emissions bands: B1 at 1.13 eV, B2 at 0.86 eV, and B3 at 1.23 eV. Based on the temperature-dependent shift of band position and the activation energy calculated out of the Arrhenius plot, the Deep Donor to Deep Acceptor (DD-DA) recombination model for Bi_2S_3 absorber films was proposed. These results so far indicate the severe limitations of the Bi_2S_3-based n-n isotype heterojunction devices with the main limitation of reduced carrier collection [37] due to the very weak built-in electric field at n-n heterojunction interface. In this regard, the implementation of alloying between Bi- and Sb-chalcogenides shows promising results from the side of the material development [49,50]. In addition, p-type doping of Bi_2S_3 remains largely unexplored [37] and research efforts for the development of p-n heterojunction Bi_2S_3 solar cells [15] can facilitate the electron-hole separation by the built-in electric field and thus increase the carrier lifetime and the performance of this emerging solar cell device.

Funding

Funding was received for this work.

Intellectual property

We confirm that we have given due consideration to the protection of intellectual property associated with this work and that there are no impediments to publication, including the timing of publication, with respect to intellectual property. In so doing we confirm that we have followed the regulations of our institutions concerning intellectual property.

Authorship

The International Committee of Medical Journal Editors (ICMJE) recommends that authorship be based on the following four criteria:

1. Substantial contributions to the conception or design of the work; or the acquisition, analysis, or interpretation of data for the work; AND
2. Drafting the work or revising it critically for important intellectual content; AND
3. Final approval of the version to be published; AND
4. Agreement to be accountable for all aspects of the work in ensuring that questions related to the accuracy or integrity of any part of the work are appropriately investigated and resolved.

All those designated as authors should meet all four criteria for authorship, and all who meet the four criteria should be identified as authors. For more information on authorship, please see http://www.icmje.org/recommendations/browse/roles-and-responsibilities/defining-the-role-of-authors-and-contributors.html#two.

We confirm that the manuscript has been read and approved by all named authors.

We confirm that the order of authors listed in the manuscript has been approved by all named authors.

CRediT authorship contribution statement

M. Koltsov: Writing – original draft, Visualization, Methodology, Investigation, Formal analysis, Conceptualization. **S.V. Gopi:** Visualization, Methodology, Investigation. **T. Raadik:** Writing – review & editing, Investigation, Formal analysis. **J. Krustok:** Writing – review & editing, Validation, Formal analysis. **R. Josepson:** Investigation, Formal analysis. **R. Gržibovskis:** Investigation, Formal analysis. **A. Vembris:** Investigation, Formal analysis. **N. Spalatu:** Writing – review & editing, Writing – original draft, Visualization, Validation, Supervision, Project administration, Methodology, Investigation, Funding acquisition, Formal analysis, Data curation, Conceptualization.

Declaration of competing interest

The authors declare that they have no known competing financial interests or personal relationships that could have appeared to influence the work reported in this paper.

Data availability

No data was used for the research described in the article.

Acknowledgments

This study was funded by the Estonian Research Council projects PSG689 "Bismuth Chalcogenide Thin-Film Disruptive Green Solar Technology for Next Generation Photovoltaics", PRG627 "Antimony chalcogenide thin films for next-generation semi-transparent solar cells applicable in electricity producing windows", and PRG1023; the Estonian Centre of Excellence project TK141 (TAR16016EK, TAR16016) "Advanced materials and high-technology devices for energy recuperation systems", and the European Union's H2020 programme under the ERA Chair project 5GSOLAR grant agreement No 952509.

Appendix A. Supplementary data

Supplementary data to this article can be found online at https://doi.org/10.1016/j.solmat.2023.112292.

References

[1] N.C. Miller, M. Bernechea, Research Update: bismuth based materials for photovoltaics, Apl. Mater. 6 (2018), https://doi.org/10.1063/1.5026541.
[2] A. Zakutayev, Brief review of emerging photovoltaic absorbers, Curr. Opin. Green Sustain. Chem. 4 (2017) 8–15, https://doi.org/10.1016/j.cogsc.2017.01.002.
[3] G. Konstantatos, L. Levina, J. Tang, E.H. Sargent, Sensitive solution-processed Bi2S3 nanocrystalline photodetectors, Nano Lett. 8 (2008) 4002–4006, https://doi.org/10.1021/nl802600z.
[4] N. Mahuli, D. Saha, S.K. Sarkar, Atomic layer deposition of p-type Bi2S3, J. Phys. Chem. C 121 (2017) 8136–8144, https://doi.org/10.1021/acs.jpcc.6b12629.
[5] C. Wadia, A.P. Alivisatos, D.M. Kammen, Materials availability expands the opportunity for large-scale photovoltaics deployment, Environ. Sci. Technol. 43 (2009) 2072–2077, https://doi.org/10.1021/es8019534.
[6] P.C.K. Vesborg, T.F. Jaramillo, Addressing the terawatt challenge: scalability in the supply of chemical elements for renewable energy, RSC Adv. 2 (2012) 7933–7947, https://doi.org/10.1039/c2ra20839c.
[7] P.J. Dale, M.A. Scarpulla, Efficiency versus effort: a better way to compare best photovoltaic research cell efficiencies? Sol. Energy Mater. Sol. Cell. (2022) 251, https://doi.org/10.1016/j.solmat.2022.112097.
[8] R. Mohan, Green bismuth, Nat. Chem. 2 (2010) 336, https://doi.org/10.1038/nchem.609.
[9] R.E. Brandt, V. Stevanović, D.S. Ginley, T. Buonassisi, Identifying defect-tolerant semiconductors with high minority-carrier lifetimes: beyond hybrid lead halide

perovskites, MRS Commun. 5 (2015) 265–275, https://doi.org/10.1557/mrc.2015.26.
[10] M.E. Rincón, M. Sánchez, P.J. George, A. Sánchez, P.K. Nair, Comparison of the properties of bismuth sulfide thin films prepared by thermal evaporation and chemical bath deposition, J. Solid State Chem. 136 (1998) 167–174, https://doi.org/10.1006/jssc.1997.7670.
[11] F. Lu, R. Li, Y. Li, N. Huo, J. Yang, Y. Li, B. Li, S. Yang, Z. Wei, J. Li, Improving the field-effect performance of Bi2S3 single nanowires by an asymmetric device fabrication, ChemPhysChem 16 (2015) 99–103, https://doi.org/10.1002/cphc.201402594.
[12] O.C. Monteiro, T. Trindade, J.H. Park, P. O'Brien, The LP-MOCVD of CdS/Bi2S3 bilayers using single-molecule precursors, Mater. Lett. 58 (2004) 119–122, https://doi.org/10.1016/S0167-577X(03)00427-0.
[13] Y.-C. Lin, M.-W. Lee, Bi2S3 liquid-junction semiconductor-sensitized SnO 2 solar cells, J. Electrochem. Soc. 161 (2014) H1–H5, https://doi.org/10.1149/2.002401jes.
[14] A.K. Rath, M. Bernechea, L. Martinez, G. Konstantatos, Solution-processed heterojunction solar cells based on p-type PbS quantum dots and n-type Bi 2S 3 Nanocrystals, Adv. Mater. 23 (2011) 3712–3717, https://doi.org/10.1002/adma.201101399.
[15] A.K. Rath, M. Bernechea, L. Martinez, F.P.G. de Arquer, J. Osmond, G. Konstantatos, Solution-processed inorganic bulk nano-heterojunctions and their application to solar cells, Nat. Photonics 6 (2012) 529–534, https://doi.org/10.1038/nphoton.2012.139.
[16] L. Whittaker-Brooks, J. Gao, A.K. Hailey, C.R. Thomas, N. Yao, Y.L. Loo, Bi2S3 nanowire networks as electron acceptor layers in solution-processed hybrid solar cells, J. Mater. Chem. C Mater. 3 (2015) 2686–2692, https://doi.org/10.1039/c4tc02534b.
[17] J. Li, X. Han, Y. Zhao, J. Li, M. Wang, C. Dong, One–step synthesis of Cu3BiS3 thin films by a dimethyl sulfoxide (DMSO)–based solution coating process for solar cell application, Sol. Energy Mater. Sol. Cell. 174 (2018) 593–598, https://doi.org/10.1016/j.solmat.2017.09.050.
[18] J. Yin, J. Jia, Synthesis of Cu3BiS3 nanosheet films on TiO2 nanorod arrays by a solvothermal route and their photoelectrochemical characteristics, CrystEngComm 16 (2014) 2795–2801, https://doi.org/10.1039/c3ce41958d.
[19] J.-J. Wang, M.Z. Akgul, Y. Bi, S. Christodoulou, G. Konstantatos, Low-temperature colloidal synthesis of CuBiS2 nanocrystals for optoelectronic devices, J. Mater. Chem. A Mater. 5 (2017) 24621–24625, https://doi.org/10.1039/C7TA08078F.
[20] S. Wang, X.Y. Liu, Y.Z. Gu, Excellent photoelectric properties and charge dynamics of two types of bulk heterojunction solar cells, Mater. Lett. 166 (2016) 251–254, https://doi.org/10.1016/j.matlet.2015.12.085.
[21] N. Spalatu, J. Hiie, R. Kaupmees, O. Volobujeva, J. Krustok, I. Oja Acik, M. Krunks, Postdeposition processing of SnS thin films and solar cells: prospective strategy to obtain large, sintered, and doped SnS grains by recrystallization in the presence of a metal halide flux, ACS Appl. Mater. Interfaces 11 (2019) 17539–17554, https://doi.org/10.1021/acsami.9b03213.
[22] T.D.C. Hobson, L.J. Phillips, O.S. Hutter, H. Shiel, J.E.N. Swallow, C.N. Savory, P. K. Nayak, S. Mariotti, B. Das, L. Bowen, L.A.H. Jones, T.J. Featherstone, M. J. Smiles, M.A. Farnworth, G. Zoppi, P.K. Thakur, T.-L. Lee, H.J. Snaith, C. Leighton, D.O. Scanlon, V.R. Dhanak, K. Durose, T.D. Veal, J.D. Major, Isotype heterojunction solar cells using n-type Sb2Se3 thin films, Chem. Mater. (2020), https://doi.org/10.1021/acs.chemmater.0c00223.
[23] F. Pattini, S. Rampino, F. Mezzadri, D. Calestani, G. Spaggiari, M. Sidoli, D. Delmonte, A. Sala, E. Gilioli, M. Mazzer, Role of the substrates in the ribbon orientation of Sb2Se3 films grown by Low-Temperature Pulsed Electron Deposition, Sol. Energy Mater. Sol. Cell. 218 (2020), 110724, https://doi.org/10.1016/J.SOLMAT.2020.110724.
[24] Y. Zhou, L. Wang, S. Chen, S. Qin, X. Liu, J. Chen, D.J. Xue, M. Luo, Y. Cao, Y. Cheng, E.H. Sargent, J. Tang, Thin-film Sb2Se3 photovoltaics with oriented one-dimensional ribbons and benign grain boundaries, 9 (2015), Nat. Photonics 9 (6) (2015) 409–415, https://doi.org/10.1038/nphoton.2015.78.
[25] S. ten Haaf, H. Sträter, R. Brüggemann, G.H. Bauer, C. Felser, G. Jakob, Physical vapor deposition of Bi2S3 as absorber material in thin film photovoltaics, Thin Solid Films 535 (2013) 394–397, https://doi.org/10.1016/J.TSF.2012.11.089.
[26] H. Song, X. Zhan, D. Li, Y. Zhou, B. Yang, K. Zeng, J. Zhong, X. Miao, J. Tang, Rapid thermal evaporation of Bi2S3 layer for thin film photovoltaics, Sol. Energy Mater. Sol. Cell. 146 (2016) 1–7, https://doi.org/10.1016/J.SOLMAT.2015.11.019.
[27] M.A. Contreras, M.J. Romero, B. To, F. Hasoon, R. Noufi, S. Ward, K. Ramanathan, Optimization of CBD CdS process in high-efficiency Cu(In,Ga)Se2-based solar cells, Thin Solid Films 403–404 (2002) 204–211, https://doi.org/10.1016/S0040-6090(01)01538-3.
[28] M. Koltsov, R. Krautmann, A. Katerski, N. Maticiuc, M. Krunks, I.O. Acik, N. Spalatu, A post-deposition annealing approach for organic residues control in TiO2 and its impact on Sb2Se3/TiO2 device performance, Faraday Discuss (2022), https://doi.org/10.1039/D2FD00064D.
[29] W. Lian, C. Jiang, Y. Yin, R. Tang, G. Li, L. Zhang, B. Che, T. Chen, Revealing composition and structure dependent deep-level defect in antimony trisulfide photovoltaics, 12 (2021), Nat. Commun. 12 (1) (2021) 1–7, https://doi.org/10.1038/s41467-021-23592-0.
[30] L.Ph Bérubé, G. L'Espérance, A quantitative method of determining the degree of texture of zinc electrodeposits, J. Electrochem. Soc. 136 (1989) 2314–2315, https://doi.org/10.1149/1.2097318.
[31] V. Piacente, V.D. Gianfreda, G. Bardi, Vapour pressure of solid Bi2S3, J. Chem. Thermodyn. 15 (1983) 7–14, https://doi.org/10.1016/0021-9614(83)90098-8.
[32] J.S. Eensalu, A. Katerski, E. Kärber, I.O. Acik, A. Mere, M. Krunks, Jako S. Eensalu, Atanas Katerski, Erki Kärber, Ilona Oja Acik, Arvo Mere, Malle Krunks, uniform Sb2S3 optical coatings by chemical spray method, Beilstein J. Nanotechnol. 10 (2019) 198–210, https://doi.org/10.3762/bjnano.10.18.
[33] P. Büttner, F. Scheler, D. Döhler, M.K.S. Barr, M. Bosch, M. Rey, T. Yokosawa, S. Hinz, J. Maultzsch, E. Spiecker, N. Vogel, I. Mínguez-Bacho, J. Bachmann, Continuous, crystalline Sb2S3 ultrathin light absorber coatings in solar cells based on photonic concentric p-i-n heterojunctions, Nano Energy 103 (2022), 107820, https://doi.org/10.1016/J.NANOEN.2022.107820.
[34] V. Kumar, E. Artegiani, P. Punathil, M. Bertoncello, M. Meneghini, F. Piccinelli, A. Romeo, Analysis of Se Co-evaporation and post-selenization for Sb2Se3-based solar cells, ACS Appl. Energy Mater. 4 (2021) 12479–12486, https://doi.org/10.1021/ACSAEM.1C02301/ASSET/IMAGES/LARGE/AE1C02301_0009.JPEG.
[35] N. Juneja, S. Mandati, A. Katerski, N. Spalatu, S. Daskeviciute-Geguziene, A. Vembris, S. Karazhanov, V. Getautis, M. Krunks, I. Oja Acik, Sb 2 S 3 solar cells with a cost-effective and dopant-free fluorene-based enamine as a hole transport material, Sustain. Energy Fuels 6 (2022) 3220–3229, https://doi.org/10.1039/D2SE00356B.
[36] I. Caño, P. Vidal-Fuentes, L. Calvo-Barrio, X. Alcobé, J.M. Asensi, S. Giraldo, Y. Sánchez, Z. Jehl, M. Placidi, J. Puigdollers, V. Izquierdo-Roca, E. Saucedo, Does Sb2Se3 Admit nonstoichiometric conditions? How Modifying the overall Se content affects the structural, optical, and optoelectronic properties of Sb2Se3 thin films, ACS Appl. Mater. Interfaces 14 (2022) 11222–11234, https://doi.org/10.1021/ACSAMI.1C20764.
[37] D. Han, M.H. Du, C.M. Dai, D. Sun, S. Chen, Influence of defects and dopants on the photovoltaic performance of Bi2S3: first-principles insights, J. Mater. Chem. A Mater. 5 (2017) 6200–6210, https://doi.org/10.1039/C6TA10377D.
[38] R. Scheer, H.W. Schock, Chalcogenide photovoltaics: physics, technologies, and thin film devices, chalcogenide photovoltaics: physics, technologies, and thin film devices. https://doi.org/10.1002/9783527633708, 2011.
[39] N. Spalatu, J. Hiie, R. Kaupmees, O. Volobujeva, J. Krustok, I.O. Acik, M. Krunks, Postdeposition processing of SnS thin films and solar cells: prospective strategy to obtain large, sintered, and doped SnS grains by recrystallization in the presence of a metal halide flux, ACS Appl. Mater. Interfaces 11 (2019) 17539–17554, https://doi.org/10.1021/ACSAMI.9B03213/ASSET/IMAGES/MEDIUM/AM-2019-032134_M018.GIF.
[40] A. Reinders, P. Verlinden, W. van Sark, A. Freundlich, Photovoltaic Solar Energy, Wiley, 2016, https://doi.org/10.1002/9781118927496.
[41] H. Shiel, O.S. Hutter, L.J. Phillips, J.E.N. Swallow, L.A.H. Jones, T.J. Featherstone, M.J. Smiles, P.K. Thakur, T.-L. Lee, V.R. Dhanak, J.D. Major, T.D. Veal, Natural band alignments and band offsets of Sb 2 Se 3 solar cells. https://doi.org/10.1021/acsaem.0c01477, 2020.
[42] X. Yu, C. Cao, H. Zhu, Synthesis and photoluminescence properties of Bi2S3 nanowires via surfactant micelle-template inducing reaction, Solid State Commun. 134 (2005) 239–243, https://doi.org/10.1016/J.SSC.2005.01.035.
[43] Y. Wang, J. feng Huang, L. yun Cao, H. Zhu, H. yan He, J. peng Wu, Preparation of Bi2S3 thin films with a nanoleaf structure by electrodeposition method, Appl. Surf. Sci. 255 (2009) 7749–7752, https://doi.org/10.1016/J.APSUSC.2009.04.163.
[44] Y. Xiao, H. Cao, K. Liu, S. Zhang, V. Chernow, The synthesis of superhydrophobic Bi2S3 complex nanostructures, Nanotechnology 21 (2010), 145601, https://doi.org/10.1088/0957-4484/21/14/145601.
[45] A. das Mahapatra, D. Basak, Enhanced ultraviolet photosensing properties in Bi2S3 nanoparticles decorated ZnO nanorods' heterostructure, J. Alloys Compd. 797 (2019) 766–774, https://doi.org/10.1016/J.JALLCOM.2019.05.160.
[46] M. Ganapathy, Y. Hsu, J. Thomas, L.Y. Chen, C.T. Chang, V. Alagan, Preparation of SrTiO3/Bi2S3Heterojunction for efficient photocatalytic hydrogen production, Energy Fuel. 35 (2021) 14995–15004, https://doi.org/10.1021/ACS.ENERGYFUELS.1C00979/ASSET/IMAGES/LARGE/EF1C00979_0011.JPEG.
[47] F. Jamali-Sheini, M. Cheraghizade, L. Heshmatynezhad, An efficient wide range photodetector fabricated using a bilayer Bi2S3/SnS heterojunction thin film, Semicond. Sci. Technol. 34 (2019), 045008, https://doi.org/10.1088/1361-6641/AB0723.
[48] J. Krustok, T. Raadik, M. Grossberg, M. Kauk-Kuusik, V. Trifiletti, S. Binetti, Photoluminescence study of deep donor- deep acceptor pairs in Cu2ZnSnS4, Mater. Sci. Semicond. Process. 80 (2018) 52–55, https://doi.org/10.1016/J.MSSP.2018.02.025.
[49] I. Caño, P. Vidal-Fuentes, A.G. Medaille, Z. Jehl, A. Jiménez-Arguijo, M. Guc, V. Izquierdo-Roca, C. Malerba, M. Valentini, M. Jiménez-Guerra, M. Placidi, J. Puigdollers, E. Saucedo, Challenges and improvement pathways to develop quasi-1D (Sb1-xBix)2Se3-based materials for optically tuneable photovoltaic applications. Towards chalcogenide narrow-bandgap devices, Sol. Energy Mater. Sol. Cell. 251 (2023), 112150, https://doi.org/10.1016/J.SOLMAT.2022.112150.
[50] T.P. Weiss, P. Arnou, M. Melchiorre, M. Guennou, D. Siopa, C. Pauly, I. Peral Alonso, P.J. Dale, S. Siebentritt, Thin-film (Sb,Bi)2Se3 semiconducting layers with tunable band gaps below 1 eV for photovoltaic applications, 024014-1–11, Phys. Rev. Appl. 14 (2020), https://doi.org/10.1103/PHYSREVAPPLIED.14.024014.